Dynamics of Underwater Gas Blowout in Sonic Regime: Laboratory-Scale Study

Huijie Wu[1]; Binbin Wang, A.M.ASCE[2]; and Anusha L. Dissanayake[3]

Abstract: To understand the dynamics of vigorous gas jets in underwater gas blowouts, we present a laboratory experiment and data analysis to quantify key physical properties of gas jets horizontally discharged through a single nozzle. This study focuses on the sonic regime of the gas jets (the nominal Mach number from 0.8 to 3.34) and quantifies the jet-to-plume transition through observations of jet penetration length, expansion angle, and trajectory of the jets. Jet penetration is found to be scaled with a modified Froude number accounting for the parameters of real gas (density, pressure, and velocity) in the choked sonic flow. The surfacing fountain profiles are measured to connect water surface observation with the source dynamics through a nondimensional scaling using the densimetric Froude number defined at the release point. A robust $-3/5$ power-law scaling with a modified Weber number is found to well characterize the median bubble diameter for the bubble breakup process in the sonic gas jets. **DOI: 10.1061/JHEND8.HYENG-13074.** *© 2022 American Society of Civil Engineers.*

Introduction

Underwater gas blowouts occur around the world and induce safety risks to offshore energy activities, including a recent gas leak causing the "eye of fire" in the Gulf of Mexico on July 2, 2021. For gas leaks with small initial velocities and flow rates, the effect of initial momentum quickly diminishes, and the flow is dominated by the buoyancy of the gas and the entrainment of ambient water into the bubble plume. There is extensive literature to document the characteristics of bubble plumes using observations, modeling, and theory developments (e.g., Ditmars and Cederwall 1974; Milgram 1983; Wüest et al. 1992; Asaeda and Imberger 1993; Simiano et al. 2006; Socolofsky et al. 2008; Dissanayake et al. 2018), with many dedicated for modeling oil and gas blowout and transport of hydrocarbon particles in both deep and shallow waters (Dissanayake et al. 2021a; Yapa and Zheng 1997; Zheng et al. 2003; Yapa et al. 2010; Dissanayake et al. 2012, 2021b; Gros et al. 2017; Johansen 2003). Under weak and moderately strong release conditions, bubble plumes can be categorized into different zones using a bubble plume length scale (Bombardelli et al. 2007; Wang et al. 2019). When gases are released at high speeds, substantial initial momentum is present, resulting in a region of the gas jet near the release point, which has unique dynamics of gas expansion, momentum change, bubble breakup, and in turn affecting the transport of discharged gases in the water column.

For gas releases from a single orifice, bubbles can behave as "bubbling" or "jetting" depending on the flow rate and the orifice diameter (Mori et al. 1982; Ozawa and Mori 1983). In the bubbling regime, the released gases behave in the format of individual bubbles or pulsating gas flows with unstable release rates. With sufficient gas flow rates, the build-up of gas puff forms as a result of the rapid deceleration of gas when entering a much denser fluid. The disturbance caused by the continuous gas release and entrainment of water breaks the gas puff into bubbles, leading to strong pressure perturbation near the release point. In the jetting regime of the flow, gas releases are in shorter time scales and behave more like a continuous jet near the source, despite the existence of pressure perturbation and gas pulsating. Mori et al. (1982) proposed the onset of gas jetting occurs at nominal Mach number $Ma \approx 1$, where Ma is defined using gas flow rate under the standard temperature and pressure (STP) condition (Q_g), cross-sectional area of the orifice (A), and the sound speed in the gas phase (a): $Ma = Q_g/(Aa)$. Numerous studies using different gases and liquids have found the onset of bubble jetting to be generally at the sonic point (Mori et al. 1982; McNallan and King 1982; Weiland and Vlachos 2013).

When gases are released beyond the sonic point, choked flows can occur and hence limit the mass flow rate even with increasing pressure at the source (Mori et al. 1982; Weiland and Vlachos 2013; Wang et al. 2018). Gas jets in the sonic regime ($Ma > 1$) has unique features. Due to the substantial density difference between the discharged gas and the receiving liquid, the gas jet can only penetrate a short distance, after which the buoyancy of the gas will dominate the flow characteristics. Hoefele and Brimacombe (1979) found the jet penetration length can be scaled with a modified Froude number and the densities of both released gas and receiving liquid must be taken into consideration. Discontinuity of the gas flow, known as pinch-off events, was found to be about 10 times the orifice diameter downstream of the gas jet with Ma from 0.4 to 1.8 (Weiland and Vlachos 2013). When gas is discharged horizontally, the effect of buoyancy bends the trajectory of the gas flow and its curvature depends on the fluxes of momentum and buoyancy. Harby et al. (2014) investigated horizontally released gas jets and fitted various empirical equations to describe the maximum pinch-off location, jet penetration length, and jet expansion angle.

Surfacing of underwater gas blowouts can threaten the stability of offshore platforms and spill-response vessels. Numerous computational fluid dynamics (CFD) modeling and integral modeling have been carried out to study the impact of bubble plumes on water surfaces. Cloete et al. (2009) used a coupled discrete phase model (DPM) and volume of fluid (VOF) method to simulate the surfacing of bubble plumes with a special treatment of initial gas momentum.

---

[1] Graduate Student, Dept. of Civil and Environmental Engineering, Univ. of Missouri, Columbia, MO 65211.

[2] Assistant Professor, Dept. of Civil and Environmental Engineering, Univ. of Missouri, Columbia, MO 65211 (corresponding author). ORCID: https://orcid.org/0000-0003-3799-2042. Email: wangbinb@missouri.edu

[3] Senior Research Scientist, SINTEF, Brattørkaia 17c, Trondheim 7010, Norway. ORCID: https://orcid.org/0000-0001-7126-4650

Note. This manuscript was submitted on September 12, 2021; approved on September 8, 2022; published online on November 10, 2022. Discussion period open until April 10, 2023; separate discussions must be submitted for individual papers. This paper is part of the ***Journal of Hydraulic Engineering***, © ASCE, ISSN 0733-9429.

J. Hydraul. Eng., 2023, 149(1): 04022034

Olsen et al. (2017) used a very large eddy simulation (VLES) to simulate the water surface velocity and depict an area of interest on the water surface where the velocity is greater than 0.1 m/s. Premathilake et al. (2016) applied their MEGADEEP model (Yapa et al. 2010) to estimate the surfacing gas flux and the location of the surfacing under ocean cross flows. On the observation side, Milgram and Burgess (1984) measured the velocity profile on the water surface caused by the bubble plume surfacing and validated the integral equations for the volume and momentum fluxes. Li et al. (2019) released gases at three different directions (horizontal, vertical, and 45°) from a 1.8 m water depth in the laboratory and found the fountain height and width are weakly correlated to the direction of the initial release but strongly correlated with the gas flow rate. Friedl and Fannel (2000) used laboratory experiments to validate their integral approach to predict the height (h_f) and width (b_f) of surface fountains: $h_f = b_s \beta \gamma Fr_s^2$ and $b_f = b_s \sqrt{1/2\beta}$ where b_s is the width of the plume at the water surface, β is an empirical coefficient accounting for the energy loss during gas surfacing, γ is the momentum amplification factor in the bubble plume, and Fr_s is the Froude number defined using the plume velocity (V_s) and width (b_s) at the water surface, $Fr_s = V_s/\sqrt{gb_s}$ with g being gravitational acceleration. These studies mainly focus on bubble plumes with low initial velocities within the subsonic regime and typically neglect jet-induced bubble breakup processes in the plume. In this study, we will measure the fountain characteristics for single-orifice gas jets under the sonic flow condition with significant bubble breakups. Particularly, we seek a simple scaling of the fountain characteristics using the parameters at the jet source, with the hope to connect the observation on the water surface to the source of gas blowouts.

In subsea oil and gas blowouts, the size distribution of the released oil droplets and gas bubbles determine their rise velocities and dissolution rates in the water column. Extensive works have been done to quantify and predict oil droplet size distribution in underwater releases. Physics-based numerical models such as the population balance method are available to predict the size distribution of oil droplets (Bandara and Yapa 2011; Zhao et al. 2015; Nissanka and Yapa 2016). On the other hand, simple scaling methods use dominant dimensionless parameters in the breakup process to estimate the characteristic size of oil droplets (e.g., median diameter d_{50}), providing efficient and acceptable estimations of the size distribution in subsea blowouts (Johansen et al. 2013; Li et al. 2017). Similar methods have been developed to predict gas bubble size distribution for underwater gas releases. Bandara and Yapa (2011) validated their population balance model in predicting bubble size distributions of the gas/liquid corelease cases in the DeepSpill experiment (Johansen et al. 2000). Zhao et al. (2016) extended their model to predict bubble sizes and recognized the importance of initial momentum using an adjustable parameter in the model. Validations of such models for high-speed gas jets do not exist mainly due to the limited data availability restricted in low gas-velocity release and gas-liquid coflow conditions (Martínez-Bazán et al. 1999; Lima Neto et al. 2008a).

A recent work of Wang et al. (2018) in a 17-m deep wave basin was the first attempt to measure bubble size distributions in underwater gas release that was made to the sonic regime. They found the median bubble diameter d_{50} converge to about 3 mm, corresponding to an Eötvös number of 1.2. Wang et al. (2018) further synthesized the data in the literature and suggested a universal scaling law for d_{50} of the underwater gas breakup under both gas-only flow and gas-liquid coflow conditions. They suggested that the bubble size should be scaled with the length scale of buoyant jets, $l_M = M^{3/4}/B^{1/2}$, where M and B are the kinematic momentum and buoyancy fluxes of the release, and the normalized bubble size should be a function of a modified Weber number. However, they were not able to resolve bubble size distributions in their small-scale water tank experiments (less than 1 m water depth) due to a significant number of gas bubbles in their vertical releases that block the optical access for size measurements. In this study, we attempt to measure bubble size distribution mainly in the sonic regime of the flow, providing additional data that extend the validation of the modified Weber number model by two orders of magnitude.

Motivated by the lack of experimental data and analysis that address various key physical processes in high-speed underwater gas leaks, this study is designed to understand, validate, and explore the dynamics of underwater gas jets at and near the release point, in the water column, and at the water surface. Specifically, we use a laboratory experiment to quantify the jet penetration length and expansion angle, trajectory of horizontal release, surfacing fountain characteristics, and bubble size distributions. Importantly, we seek a universal scaling relationship of these key parameters based on their physical dominant processes, with the aim of synthesizing knowledge and guiding predictions for responding to underwater gas leaks and blowouts.

Experimental Setup

The experiment was conducted in an ultra-clear glass water tank ($2 \times 1 \times 1$ m^3) located in the environmental fluid dynamics laboratory at the University of Missouri. The tank was filled with fresh water at room temperature (about 22°C). Compressed air was released from two small-diameter nozzles (4 and 8×10^{-4} m) at 0.4 m below the water surface. Gas was supplied from a standard gas and vacuum system in the laboratory and released horizontally from the nozzle mounted on an 80/20 Aluminum platform (Fig. 1). The discharge of gas was controlled by a needle valve and the flow rate was measured using a mass-based flow meter (OMEGA Engineering). Five cases with different discharges and nozzle diameters were conducted, with the nominal Mach number from 0.83 to 3.34 (see Table 1 for details of the experimental parameters).

Two cameras were placed on one side of the tank to take shadow-graphic images. Two 350-W halogen lamps and a 60-W LED lamp with a translucent screen were used as the back-light source. A high-speed camera (Phantom VEO 440L) was used to observe the behavior of gas jets immediately discharged into water, spatial distribution of bubbles while rising in the water, and bubble size distribution. The 72GB built-in memory in the camera limits the measurement duration of each case. For 0.4 mm nozzle cases (N1 cases), image resolution was set to $1{,}152 \times 1{,}600$ pixel^2, resulting in 27,568 images for each case. With a sample rate of 24 frame-per-second (fps), the measurement duration was about 19 min. For 0.8 mm nozzle cases (N2 cases), image resolution was $1{,}920 \times 1{,}600$ pixel^2. 16,546 images were obtained within the measurement duration of about 11.5 min at 24 fps. In addition, we applied a high sample rate (19,000 fps) to the N2 cases to observe the evolution of jet dynamics immediately after the discharge.

A USB 3.0 camera (Basler ace acA1300-200um) was used to observe the interaction of the bubble plume with the water surface. 24 fps was used to obtain images for 5 min at the air-water interface, giving 7,200 images at $1{,}280 \times 1{,}024$ pixel^2 for each case. Fig. 1 shows the experimental setup and sample images from each camera.

Data Processing

Cross-Sectional Void Fraction and Trajectory

Void fraction is defined as the percentage of occupation duration by gas phase in bubbly flows, which is typically measured using

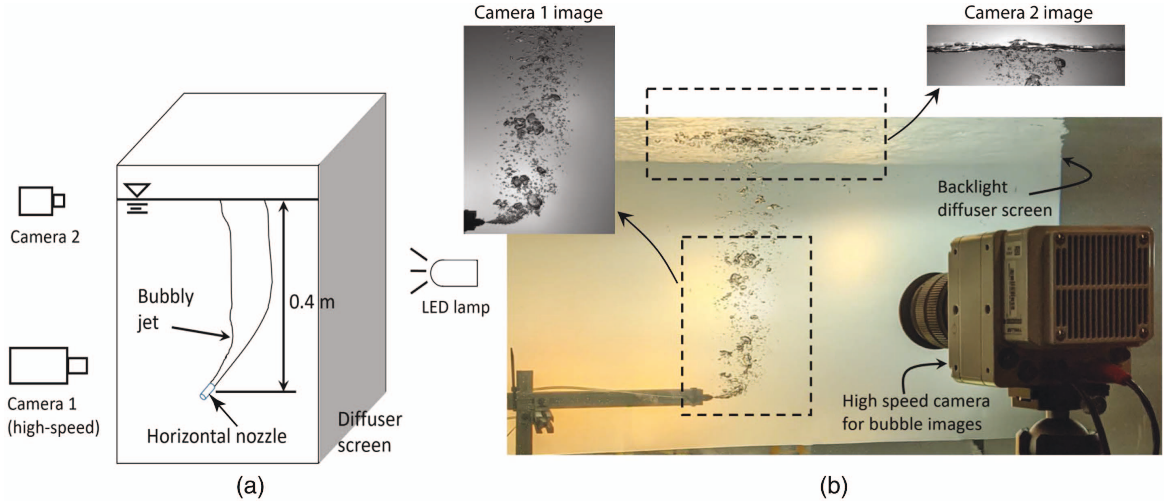

Fig. 1. (Color) Setup of the bubble jetting experiment: (a) sketch of the setup; and (b) photo of the setup. Sample image of each camera is inserted.

Table 1. Parameters of experimental conditions and gas flows

	Case				
Parameter	N1Q1	N1Q2	N2Q1	N2Q2	N2Q3
Nozzle diameter (mm)	0.4	0.4	0.8	0.8	0.8
Gas flow rate at STP (L/min)	2.2	4.4	10.6	21.2	35.6
Nominal gas flow velocity (m/s)	280.9	561.8	338.4	676.7	1,136.4
Nominal Mach number	0.83	1.65	1.00	1.99	3.34
Reynolds number	7,800	16,000	19,000	37,000	63,000
Jet penetration distance (cm)	3.1	3.8	3.8	6.2	8.0
Jet expansion angle (degrees)	21.6	24.1	19.7	17.5	18.4
Fountain height (cm)	1.84	2.55	4.23	6.22	7.09
Fountain half-width (cm)	5.68	8.52	10.52	12.34	13.90

intrusive probes including conductive probes and fiber optical probes (e.g., Chanson 2002; Lim et al. 2008). Quantitative imaging is an alternative, nonintrusive method to measure void fraction in bubbly flows (Simiano et al. 2006; Seol et al. 2007). Because the bubble images are two-dimensional projections of the bubbly flow onto the imagery plane, the optically measured void fraction is an integrated cross-sectional void fraction (Wang et al. 2019; Wu et al. 2021; Li et al. 2020). Despite its two-dimensional representation of the gas flow, appropriate scaling can be used to convert the cross-sectional void fraction into the local void fraction defined as the percentage of duration occupied by the gas phase in two-phase flows (Wu et al. 2021).

Image processing for back-light shadow-graphic imagery is straightforward and has been previously applied to bubble plumes in both laboratory and field experiments (Wang et al. 2016; Li et al. 2020). We first applied a 3×3 "sobel" filter to enhance the gradient of intensity in the image that was then converted to the binary image using a global threshold. The holes in the binary images were filled using a 4-connectivity method, where the value of '1' represents gas and '0' represents liquid. A sample image and the results of image processing are given in Fig. 2. The cross-sectional void fraction (χ_{cs}) can be calculated by counting the percentage of gas occupation at each pixel over the entire dataset. Figs. 2(b and c) show the calculated cross-sectional void fraction after averaging data from 20 images and all images, respectively. The trajectory of the jet can then be estimated from the void fraction distribution, defined by the location of the maximum void fraction in each cross section of the jet [Fig. 2(c)].

Jet Penetration Length and Expansion Angle

Jet penetration length (l_p) represents the relative importance of the initial jet momentum and the buoyancy (Hoefele and Brimacombe 1979; Harby et al. 2014). l_p is defined as the horizontal distance from the location of the nozzle to the turning point of the bending jet. Hoefele and Brimacombe (1979) used the intercept between the centerline of the jet and the horizontal plane of the nozzle using high-speed imagery. Harby et al. (2014) used the intercept between the nozzle plane and the sharpest intensity gradient line after averaging 13-s images. Here we use the result of the cross-sectional void fraction χ_{cs} to define the jet envelope at $\chi_{\mathrm{cs}} = 80\%$, which intercepts the nozzle plane to define the jet penetration length. Fig. 3 shows the determination of the jet penetration length for each case. From the images, the jet expansion angle can be estimated by calculating the tangible line of the 80% void fraction at the nozzle.

Surfacing Fountain Profile

The profiles of the surfacing fountain were determined from the shadow images captured at the air-water interface, see Fig. 4(a) for a sample image. We first calculated the minimal and maximal intensity at each pixel over the entire dataset and smoothed the intensity value using a 50-pixel moving average in the vertical direction (each column of the image matrix). The intensity gradient was then computed for each pixel column of the minimal intensity and the maximal intensity matrices. The fountain boundary at the air-water interface should exhibit a negatively peaked gradient and a positively peaked gradient in the minimal and maximal intensity images, respectively (see 4b for the plot of gradient curves). We combine these two curves by subtracting the intensity gradient values between the maximal and minimal intensity images and determining the fountain location where the final gradient curve approaches 95% of the peak value in the downward direction. The fountain profile was then smoothed using a 50-pixel moving average to obtain the final result. Figs. 4(c and d) show the calculated fountain profile for the case N1Q1 (i.e., Nozzle 1, flow rate 1)

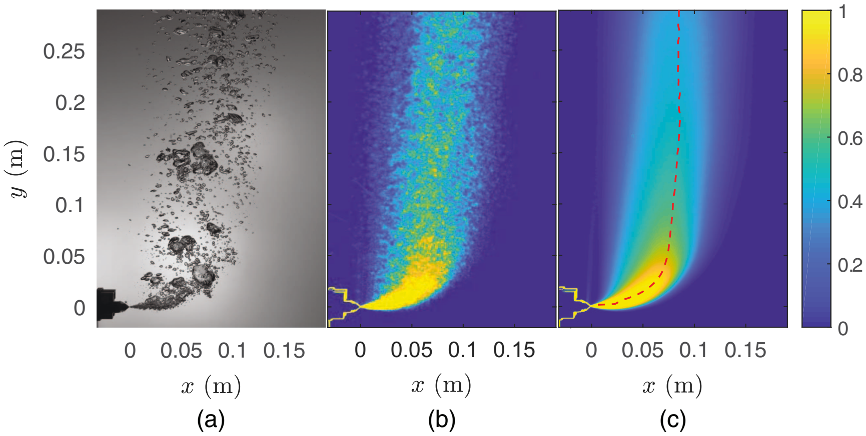

Fig. 2. (Color) (a) A sample image for $Q = 4.4$ L/min and $D = 0.8$ mm; (b) cross-sectional void fraction distribution with 20 images; and (c) cross-sectional void fraction distribution using the entire dataset (27,568 images). The trajectory of the jet is shown as a red dashed line. The color bar shows the value of the void fraction.

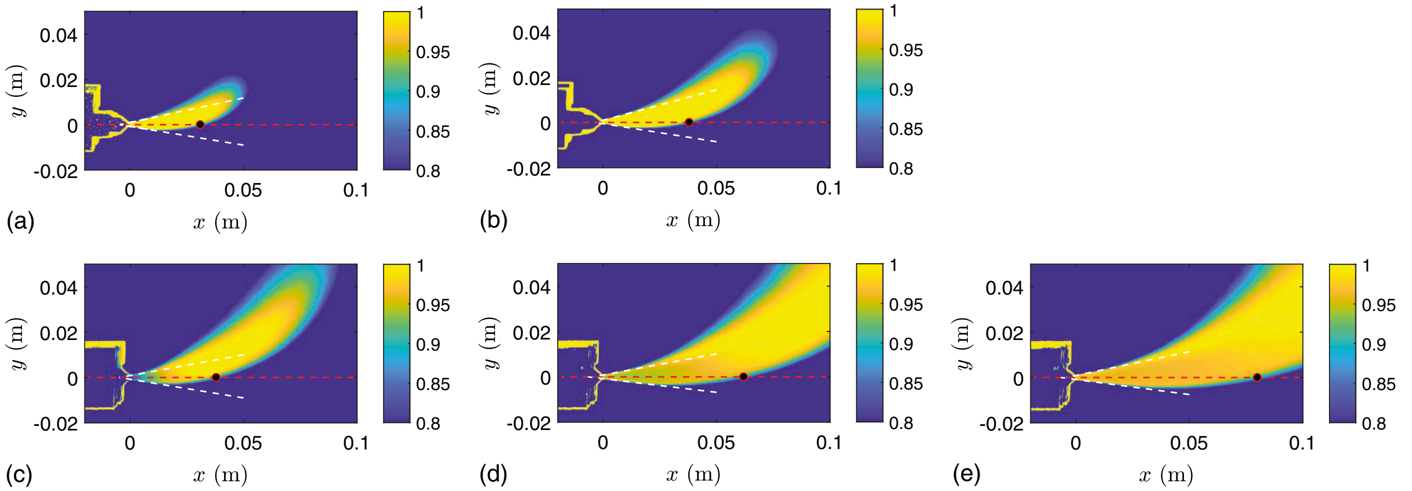

Fig. 3. (Color) Jet penetration length and jet expansion angle: (a) N1Q1; (b) N1Q2; (c) N2Q1; (d) N2Q2; and (e) N2Q3.

superimposed onto the minimal and maximal intensity images, respectively. Visually examination confirms that the fountain profile aligns well with the images. Once the fountain profiles are determined, fountain height (h_f) and fountain half-width (b_f) can be calculated by fitting a Gaussian equation to the profile, such that: $h/h_f = \exp(-(x^2)/(b_f^2))$ (see later Fig. 9). Physically, fountain height is the maximal height of the water-upwelling induced fountain profile relative to the still water surface, and fountain half-width is a characteristic width of the profile.

Bubble Size Distribution

Bubble size distribution can be obtained by separating individual bubbles using image processing (Wang and Socolofsky 2015a). Even with relatively sophisticated algorithms to identify the overlapped bubbles, the traditional image processing method only works well for low void fraction conditions. For the images of gas jets in this work, there are significant bubble overlaps when large bubbles are present. Hence, we manually mark these bubbles in addition to the automated image processing (Fig. 5).

To estimate bubble size distribution, we first select a region of interest with a height of 13.5 cm about 15 cm away from the nozzle (375× and 188× nozzle diameter for N1 and N2 cases, respectively) to exclude the initial bubble breakup region. Small bubbles are identified using a bubble size threshold combined with a roundness threshold (Wang and Socolofsky 2015a). For large, overlapped bubbles, the boundary of each bubble was marked using 10 manually clicked points, which were used to fit an ellipse (Fig. 5). The equivalent spherical diameter was then estimated from the fitted major and minor axes: $d = (a^2 b)^{1/3}$ (Wang and Socolofsky 2015b). Due to the extensive time requirement and labor, limited data sets were processed for each case, and the numbers of processed bubbles are summarized in Table 2.

Results and Discussion

Qualitative Description of the Submerged Gas Jets in Sonic Regime

The gas jet exhibits strong instability immediately after the discharge (see Videos S1–S3). Pulsating behavior was observed in all cases although the gas jets are classified as jetting (Mori et al. 1982). This is due to the compressibility of gas and a large density

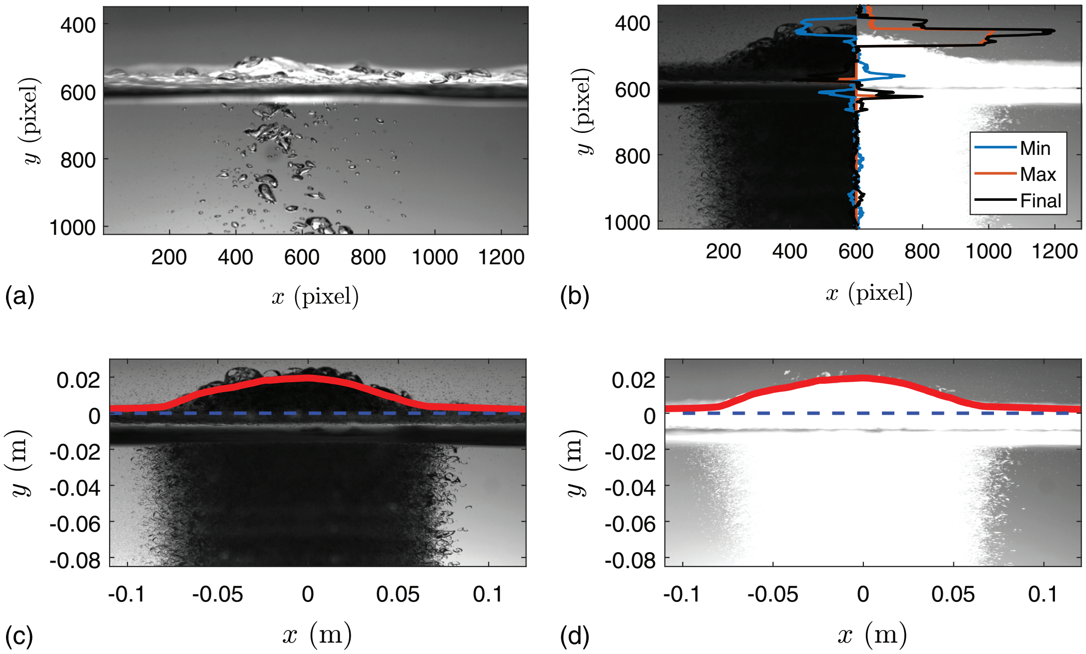

Fig. 4. (Color) (a) A sample image of bubble surface interaction for the case N1Q1: $Q = 2.2$ L/min and $D = 0.4$ mm; and (b) an example of image processing to identify the fountain profile. Legend shows the intensity gradient curve at the 600-pixel column for minimal intensity figure ("Min"), maximal intensity image ("Max"), and the final gradient curve ("Final"). (c and d) Image processed fountain profile (red solid curve) above the water surface (blue dashed line). The profile is superimposed onto the minimal greyscale intensity image in subplot c and the maximal greyscale intensity image in subplot (d).

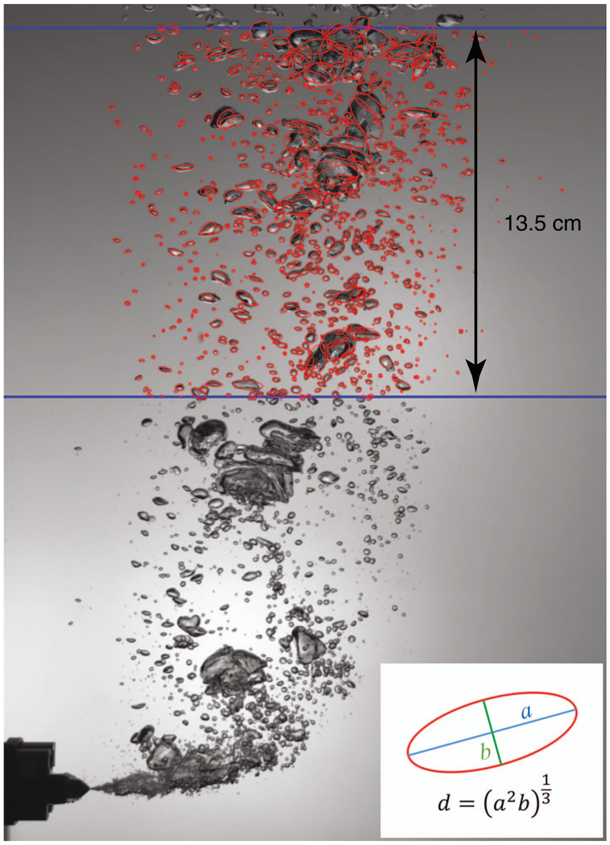

Fig. 5. (Color) Image processing for bubble size measurements. The lower-right insert shows the calculation of the equivalent spherical diameter from the ellipse fitting.

difference between the gas and the receiving liquid, which has been well-observed in literature (McNallan and King 1982; Zhao and Irons 1990; Weiland and Vlachos 2013). Pinch-off events were observed for low Ma cases as a result of instability in the jet (Fig. 6). Weiland and Vlachos (2013) reported that the pinch-off events occurred at the distance within $10l_q \sim 15l_q$ or equivalently $8.9D \sim 13.3D$ in their jets with $Ma = 0.4 \sim 1.1$, where l_q is the characteristic length scale of a pure momentum jet (Fischer et al. 1979). The pinch-off distance in Fig. 6 is within $9.5D \sim 12.9D$ and the pinch-off duration is about 3.68 ms. Using Figs. 6(b–h), we can estimate the speed of gas expansion in this pinch-off event to be about 4.3 m/s. Weiland and Vlachos (2013) reported the broadest locations of pinch-off events at $Ma = 0.4$ and no pinch-off events at $Ma = 1.8$ in their vertical gas jets. In our experiment, pinch-off events were not observed for N2Q2 ($Ma = 1.99$) and N2Q3 ($Ma = 3.34$), and the continuity (smoothness) of the gas discharge increased with increasing Ma.

Jet Penetration Length and Expansion Angle

Jet penetration length (l_p) has a positive correlation with gas momentum flux (M_g) for each nozzle diameter, shown in Fig. 7(a), plotted with the data reported in Harby et al. (2014). For the same nozzle, the initial momentum is the dominant parameter to determine the jet penetration length. Because l_p can be considered as a characteristic length of the transition from the momentum dominant regime to the buoyancy dominant regime, the impact of buoyancy force is implicitly shown in Fig. 7(a), giving different trends of the l_p-M_g relationship.

Harby et al. (2014) suggested using a nozzle Froude number $Fr = V_0/\sqrt{g(\Delta\rho/\rho_g)D}$ to scale with the jet penetration length, where V_0 is the gas velocity at the nozzle, D is the nozzle diameter, g is the gravitational acceleration, ρ_g is the gas density at the nozzle,

Table 2. Parameters of bubble size distribution

	Case				
Parameter	N1Q1	N1Q2	N2Q1	N2Q2	N2Q3
Number of processed bubbles	1,036	1,111	1,594	1,836	2,795
Bubble median diameter in population (mm)	1.78	2.20	1.96	2.26	2.14
Bubble median diameter in volume[a] (mm)	6.57	7.21	6.79	6.63	6.07
Maximal bubble diameter (mm)	59.29	144.20	95.76	212.73	317.31
Minimal bubble diameter (mm)	0.45	0.45	0.44	0.44	0.44

[a] Bubbles with diameter $d_{cr} > 10$ mm are removed.

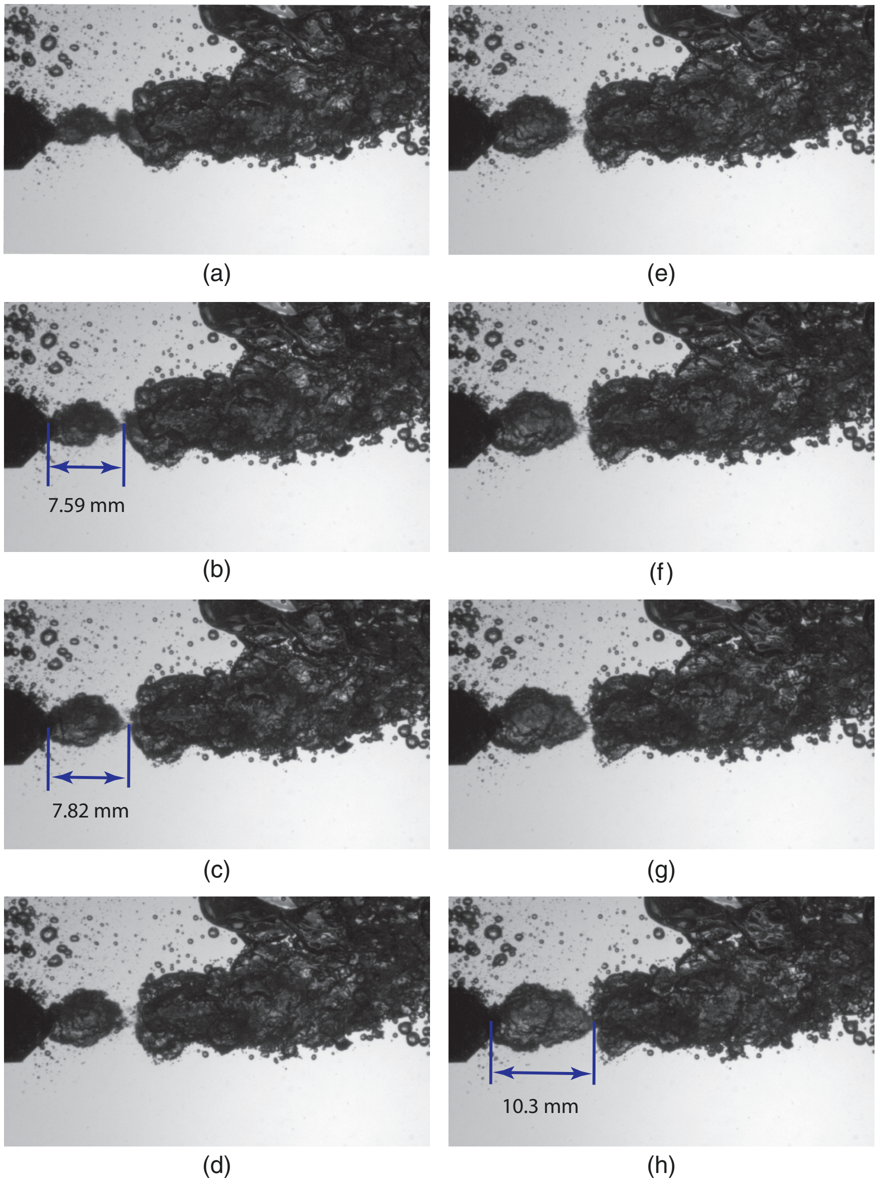

Fig. 6. (Color) A pinch-off event in the case N2Q1 with a pinch-off duration of about 5 ms (b–g). The time interval between each of the two consecutive images is approximately 1.053 ms (i.e., every other image in the recorded data): (a) $t = 0$ ms; (b) $t = 1.053$ ms; (c) $t = 2.105$ ms; (d) $t = 3.158$ ms; (e) $t = 4.211$ ms; (f) $t = 5.263$ ms; (g) $t = 6.316$ ms; and (h) $t = 7.368$ ms.

and $\Delta\rho$ is the density difference between gas and liquid. They proposed a power-law relationship between normalized l_p and Fr_0: $l_p/l_q = c_1 Fr_0^{c_2}$ with fitted parameters $c_1 = 2.29$ and $c_2 = 0.61$. In their experiments, most cases had $Ma < 1$ where the gas density was close to its value at the hydrostatic pressure condition at the nozzle, and the real gas exit velocity was close to its nominal value calculated at the STP condition. Our experiments span a range of Ma between 0.83 and 3.34 and the gas flows were choked in most conditions. Therefore, the fitted equation from low Ma experimental data does not agree with the data measured in our experiments.

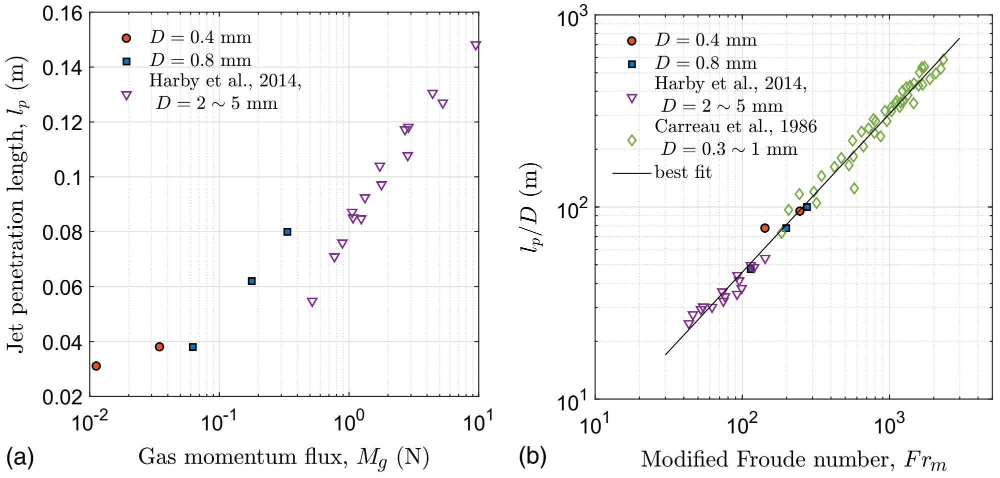

Fig. 7. (Color) (a) Measured jet penetration length (l_p) as a function of gas momentum flux (M_g); and (b) scaling of jet penetration length using modified Froude number, where l_p is normalized using nozzle diameter D. The available data from (Harby et al. 2014) and (Carreau et al. 1986) were digitized from their figures and recalculated to be included in the plot.

For gas jets in the sonic regime, Mori et al. (1982) suggested the real gas exit velocity should be calculated as

$$V_g = \begin{cases} a\left(\dfrac{-1+\sqrt{1+2(\kappa-1)Ma^2}}{(\kappa-1)Ma}\right) & \text{for } Ma < \sqrt{(\kappa+1)/2} \\ a\sqrt{\dfrac{2}{\kappa+1}} & \text{for } Ma \geq \sqrt{(\kappa+1)/2} \end{cases} \tag{1}$$

where a = sound speed in the gas phase; and κ = specific heat ratio C_p/C_v of the gas.

The pressure at the nozzle exit is given by

$$P_g = \begin{cases} P_0 & \text{for } Ma < \sqrt{(\kappa+1)/2} \\ P_0 Ma\sqrt{\dfrac{2}{\kappa+1}} & \text{for } Ma \geq \sqrt{(\kappa+1)/2} \end{cases} \tag{2}$$

From Eqs. (1) and (2), the sonic point is the criterion in determining the flow regime: increasing Ma leads to an increase of exit velocity with constant pressure in subsonic conditions ($Ma < \sqrt{(\kappa+1)/2}$), whereas increasing Ma only increases the gas pressure at the nozzle and the exit velocity maintains a constant value in the sonic condition ($Ma \geq \sqrt{(\kappa+1)/2}$).

In the sonic regime, the density of gas at the nozzle can be calculated as

$$\rho_g = \frac{\kappa P_g}{a^2} \tag{3}$$

With these parameters, we use a modified densimetric Froude number Fr_m to include the correct pressure and velocity of the gas jet in the sonic regime

$$Fr_m = \sqrt{\frac{\rho_g V_g^2 + (P_g - P_0)}{(\rho - \rho_g)gD}} \tag{4}$$

Here, the modified Froude number takes into consideration the pressure difference before and after gas expansion from the nozzle to the receiving water (Carreau et al. 1986). Fig. 7(b) plots the normalized jet penetration length using nozzle diameter against Fr_m, where the literature data from Harby et al. (2014) and Carreau et al. (1986) were digitized from their figures and recalculated. This plot shows a universal relationship (best-fit line: $l_p/D = 1.03Fr_m^{0.82}$) across a large range of nozzle diameters ($0.3 \sim 5$ mm) in both subsonic and sonic regimes in three independent experiments.

Jet penetration length can be analogous to the horizontal distance of the potential core of horizontally released single-phase buoyant jets. Lee and Chu (2003) used numerical simulation data to show the potential core length $z_e \approx 6D$ for $Fr = 20$, less than $5D$ for $Fr = 2$, and less than $3D$ for $Fr = 0.1$. Despite the unclear quantitative relationship between Fr and the potential core length, a positive correlation between Fr and z_e is observed, which is similar to what we report here for horizontal gas-only jets. We note orders of magnitude difference in Froude number between our gas jets and single-phase buoyant jets; however, extrapolation of our Fr versus jet penetration relation seems to provide the same order of magnitude estimation for those reported values.

The jet expansion angles θ were found to be in the range of 17.5° and 24.1° with no obvious trend with the variation of nozzle diameter and the gas flow rate. Harby et al. (2014) found increasing jet expansion angle (approximately $6° \sim 12°$) with increasing flow rate under the conditions of nozzle diameter $D = 2 \sim 5$ mm and $Ma = 0.59 \sim 1.06$. Carreau et al. (1986) reported $20° \sim 30°$ in their nitrogen jets in water and suggested a boundary value of 25° for the sonic jet.

Jet Trajectory

The measured trajectories of gas jets for all cases were shown in Fig. 8. The location of the trajectory at about 25 cm above the release height extends from 6 to 19 cm from the lowest to the highest flow rates. To validate the prediction of gas trajectory, we follow the momentum equation proposed by Themelis et al. (1969) and outlined in Carreau et al. (1986) to calculate the trajectories of the gas jets. The trajectory equation reads

$$\frac{d^2\hat{y}}{d\hat{x}^2} = 4\chi_0 Fr_m^{-2}\tan^2\left(\frac{\theta}{2}\right)\sqrt{1+\left(\frac{d\hat{y}}{d\hat{x}}\right)^2}\,\hat{x}^2 \tag{5}$$

where $\hat{y} = y/D$ and $\hat{x} = x/D$ = normalized coordinates; χ_0 = void fraction in the jet after the gas expansion, which is defined in the

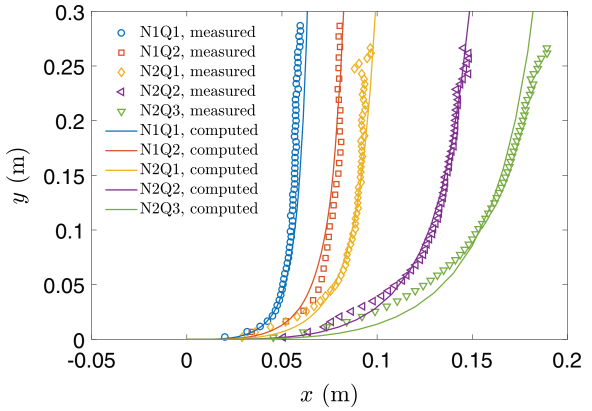

Fig. 8. (Color) Trajectories of the gas jets. $(x, y) = (0, 0)$ represents the jet nozzle location.

mass balance equation accounting for the entrainment of ambient water into the jet: $\left[(\pi d_{\text{jet}}^2)/(4)\right]\chi_0\rho_0 V_{\text{gas}} = [(\pi D^2)/4]\rho_g V_g$.

Fr_m and θ in Eq. (5) are resolved and calculated from image processing. Calculating χ_0 requires the knowledge of water entrainment at the jet source and the gas velocity in the jet (V_{gas}), which requires measurements of the velocities of both gas and water. Carreau et al. (1986) combined the geometry of the jet with multiple assumptions and an empirical slip ratio of the water and gas velocity to determine the void fraction. Here we estimated the void fraction by solving Eq. (5) using the fourth-order Runge-Kutta method and found $\chi_0 = 0.5$ and 0.7 from the measured trajectory for $D = 0.4$ mm and 0.8 mm, respectively. The results of calculated trajectories are plotted in Fig. 8. The good agreement between the measurement and calculation suggests that the curves of the gas jets are well described by the governing equation to account for the combined effect of initial discharge momentum and the buoyancy of the discharged gas. The calculation should be carried out using appropriately determined gas density, pressure, and velocity under the sonic conditions, as well as the estimated value for the void fraction. We note that validating the void fraction at the jet source location is subject to future investigation of water entrainment. This will allow it to be used as a standalone function to initialize models of the pure gas blowout in the release velocity regimes considered here.

Surface Fountain

The profiles of surface fountains for all cases are shown in Fig. 9(a). The measurement results show a increasing fountain height and width with increasing gas flow rate. Despite the irregularity of the profile, all profiles show a relatively good symmetry about the center of the fountain under the horizontal gas release conditions. This indicates the gas flows are dominated by the buoyancy force and the influence of the direction of initial momentum may be small for the profiles of surface fountains. The symmetric surface profile also suggests that the entrainment of ambient water is equally efficient on both sides of the bubbly flow.

Fig. 9(b) shows the plot of fountain height and half-width as a function of gas flow rate, where h_f and b_f are determined from the Gaussian fitting. Using power-law fit, we found: $h_f = 3.25Q^{0.51}$ and $b_f = 1.39Q^{0.30}$. Because the horizontal dimension of the fountain is the result of water entrainment in the plume, the size of the fountain would change with the depth of release. Friedl and Fannel (2000) suggested the fountain profiles should be scaled with the Froude number defined by the parameters of the bubble plume at the water surface: $Fr_s = V_c/\sqrt{gb}$ where V_c is the plume centerline velocity and b is the plume half-width at the location of the water surface. For bubble plumes with low initial momentum, the prediction of V_c and b can be obtained by solving integral equations of mass and momentum conservation with an appropriate entrainment model and initial condition (Socolofsky et al. 2008; Dissanayake et al. 2018).

To examine the relationship between the fountain profile and the source dynamics, we test the scaling of the h_f and b_f with the densimetric Froude number $Fr = \sqrt{(\rho V_0^2)/(\rho - \rho_0)gD}$ based on gas release conditions. Considering $h_f \sim Q^{0.51}$, $b_f \sim Q^{0.30}$ and using the definition of Q and Fr, we derive the scaling relationships: $h_f H^{1/4} D^{-5/4} \sim Fr^{1/2}$ and $b_f H^{-0.25} D^{-0.75} \sim Fr^{0.3}$. Here H is the release depth and is used as a dummy variable in the normalization so that the power of D can be set to match the relationship between Q and the fountain parameters h_f and b_f. The plot of data on the scaling relationship and the best-fit lines are shown in Fig. 10. Good agreements are found in the data to support this scaling in our experimental conditions. We note that the fountain profile is the result of water entrainment in the rising plume and hence should be positively related to the release depth. The quantitative influence of H in scaling must be related to the volume fluxes of ambient water entrainment in the bubble plume.

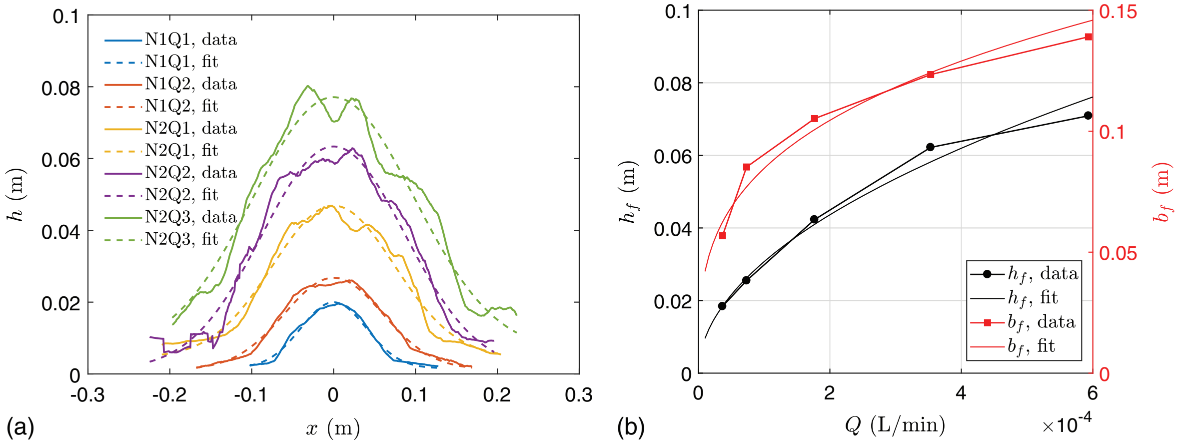

Fig. 9. (Color) (a) The profile of the fountain for all cases, with the comparison to Gaussian fit; and (b) Fountain height (h_f) and fountain half-width (b_f) as a function of gas flow rate.

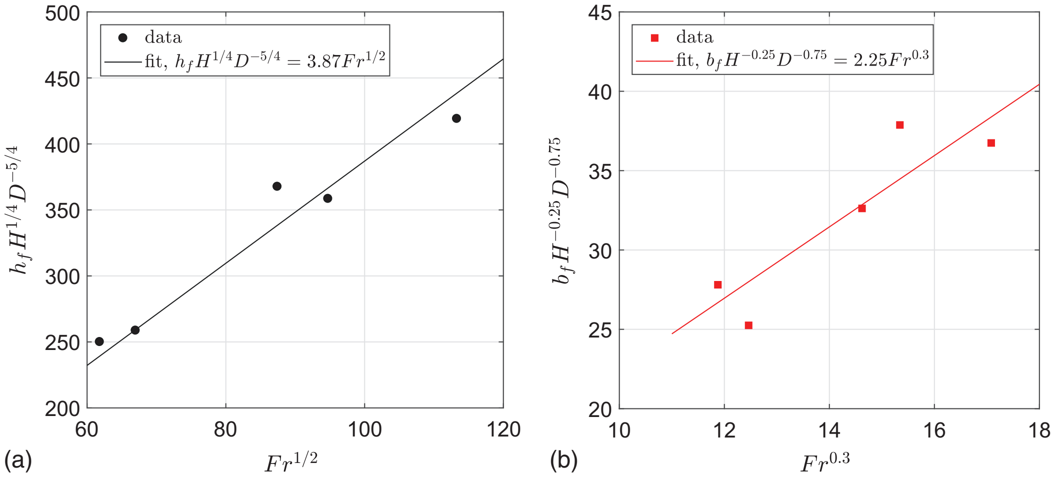

Fig. 10. (Color) Normalized fountain characteristics with Fr: (a) fountain height; and (b) fountain half-width.

Bubble Size Distribution

The discharged gases start to break up into small bubbles due to the strong shear caused by the momentum changes and the turbulence in the jet regime. From the images, we observed many small spherical and ellipsoidal-shaped bubbles above the jet regime. A few large ones have significant deformation and sometimes break up into small bubbles while rising in the water column (Fig. 5). The probability density function of the bubble sizes based on volume is heavily tail skewed due to these large bubbles (not shown here). Because their breakup is a continuous process within the shallow water depth in the laboratory experiment, we have removed all bubbles that are large than a critical diameter of $d_{cr} = 10$ mm in calculating statistics based on bubble volume, suggested by the maximal stable bubble diameter due to the Raleigh stability criterion, i.e., $d_{max} = 4\sqrt{\sigma/(\Delta\rho g)} \approx 10$ mm (Clift et al. 1978). We note that the actual maximal bubble sizes can be much larger than 10 mm (Grace et al. 1978; Wang et al. 2018), and these large bubbles were observed in our experiment. These bubbles are quite unstable and may be broken up into smaller bubbles while rising in the flow. In our data, these large bubbles contribute only a small portion of the population (less than 1%) after the atomizing breakup. However, they may contribute a major volume fraction (1% to 80% in our experiment) and will experience a secondary breakup mechanism when they rise up. The process of secondary breakup of these large bubbles was not quantified in our experiment due to shallow water depth. Hence, these large bubbles should be treated separately when considering mass transport in the water column. Here, we focus on the distribution of atomized bubbles immediately after the release.

The measured atomized bubble size distribution is plotted in Fig. 11 in the format of cumulative probability distribution function (CDF) based on the population and the volume (Wang et al. 2016). The data show very similar distributions of bubble sizes and quite consistent median bubble diameters (d_{50}) regardless of the nozzle diameter and flow rate (see Table 2). Consistent median bubble diameters and size distributions were observed in the experiment with much larger nozzles (3 ~ 8 cm) and flow rates (0.23 ~ 0.77 m^3/s under STP conditions) (Wang et al. 2018). A data synthesis study by Wang et al. (2018) shows a converged bubble size at Eötvös number (Eo) of 1.2. However, our experiment shows one to two orders of magnitude larger Eo. Wang et al. (2018) suggested $Eo = 1.2$ may not be universal due to the narrow range of turbulent breakup regimes in the available data, and our new data indeed confirm this hypothesis.

The data synthesis by Wang et al. (2018) found a universal $-3/5$ power-law scaling relationship between bubble characteristics size and a modified Weber number. The $-3/5$ scaling law has only been validated in the subsonic regime with one data point in the sonic

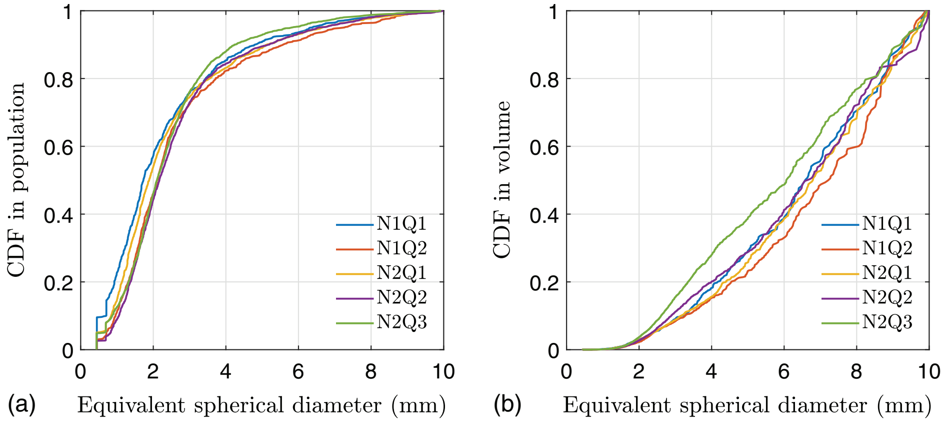

Fig. 11. (Color) CDF of measured bubble size distribution after removing bubbles that are greater than 10 mm in diameter: (a) CDF in population; and (b) CDF in volume.

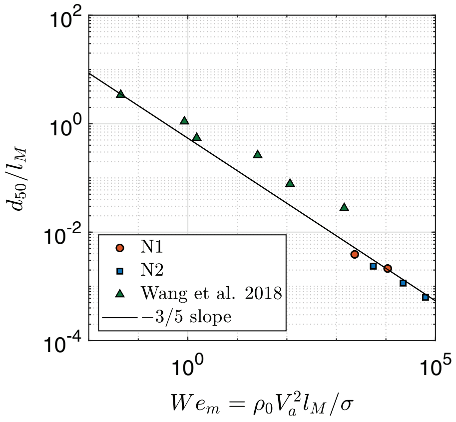

Fig. 12. (Color) Scaling of median bubble diameter with modified Weber number. The solid line shows the best-fit line for two separated data sets according to the $-3/5$ law $d_{50}/l_M = 0.54We_m^{-3/5}$.

regime. To test the Weber number scaling for the underwater gas blowout, Fig. 12 depicts the measured bubble size in the normalized parameter space, along with the data from the large wave basin experiment by Wang et al. (2018). Our data closely follow the $-3/5$ law of Weber number scaling. The data in our study and by Wang et al. (2018) span at least one order of magnitude in nozzle diameter and flow rate, as well as the Reynolds number and Weber number in the nondimensional parameter space. This suggests a robust Weber number scaling for bubble breakup in underwater gas blowouts in the sonic flow regime. Our data lie in the atomization stage of bubble breakup, i.e., $We_m > 324$, where the bubble breakup is due to the actions of turbulent eddies (Masutani and Adams 2001; Wang et al. 2018). This mechanism of the bubble breakup agrees with the observation: most bubbles break up within a short distance after the release, only a few large ones leave the primary breakup region; therefore, their secondary breakup would likely be controlled by the combination of the Raleigh instability and the turbulence within the plume.

The $-3/5$ law represents the physical mechanism of the breakup of immersible fluid particles in turbulent flows, i.e., fluid particle breakup is a balance between a destructive force from turbulent kinetic energy and a resisting force from interfacial tension. As a result, the maximal bubble diameter can be determined using dimensional analysis with key parameters, i.e., turbulent dissipation rate, density of fluids, interfacial tension, and viscosity (if viscous force is more important than interfacial tension) (Hinze 1955; Johansen et al. 2013). The $-3/5$ Weber number scaling was first used for oil droplets and later extended for gas bubbles with modification of the length scale based on the flow regime (Wang et al. 2018). Our data here further validate this scaling mechanism in a wider application range. Because this scaling only takes the parameters of the source condition, it can be easily implemented in predicting initial bubble sizes in an underwater gas blowout with an appropriate size distribution assumption (e.g., log-normal distribution). Reliable prediction of bubble sizes is necessary to provide critical initial conditions for the transport and fate models in subsea blowouts.

Discussion on Underwater Blowouts and Gas Leakages

Underwater gas blowouts and leakages could occur during the installation of oil/gas explorations, and pipeline transport of CO_2 or natural gases. Sonic gas flows could occur from a small crack with an adequate pressure difference between the pipeline and the ambient water. The experimental data and analysis presented in this paper may provide some insights regarding how the initialization of gas blowouts and leakages should be modeled. We demonstrate the dynamic behavior of the gas jets in the vicinity of the nozzle, which is key to the transition of flow regimes and the breakup of the gas bubbles. Our study shows the necessary modification of dimensionless numbers (i.e., Weber number) is needed to scale flow parameters if gas release velocity is adequately high. Hence, careful examination of the source condition and its impact on the flow characteristics in the immediate vicinity of the source must be considered in simulating underwater gas blowouts. Traditional integral models for buoyant jets and plumes may only be valid after the completion of gas expansion in high-speed gas blowouts where the flow is primarily driven by buoyancy.

The physics presented here is applied to gas-only releases, and the induced flow is solely controlled by escaping gas. As discussed, the flow dynamics is initially controlled by the gas jet due to high initial velocity and then transitions to a bubble plume after the gas expansion and momentum exchange between the gas and surrounding water, which occurs on the scale of jet penetration length. In oil well blowouts like Deepwater Horizon, oil and hydrocarbon gases can be released from the same source. In such oil/gas coflows, the characteristics of flow must be parameterized using both phases. Because oil has a much larger density and hence carries much larger dynamic momentum than the released gas with the same volume flux, it is likely that most oil/gas coflows are dominated by oil-induced jets and/or plumes. Hence, assumptions of neglecting the influence of gas on the flow characteristic may be justified. However, when the gas phase contributes a nonnegligible mass flow rate, the influence of the gas phase must be considered.

Observational Uncertainty

We expect that some large-scale circulations occur in the tank. These tank-size motions can change the meandering frequency of the bubble plume and also affect the water velocity within the plume (Lima Neto et al. 2008b). However, our analysis focuses on the jet region where the effect of large-scale motion is negligible. The accuracy of bubble size measurements depends on the bubble deformation and overlap of bubbles in two-dimensional images. Quantification of deformed bubbles has been a challenge in optical methods, and recent developments in machine learning algorithms may provide alternative solutions to improve measurement accuracy (e.g., Kim and Park 2021; Hessenkemper et al. 2022).

Summary and Conclusions

In this paper, we conducted a laboratory experiment to study the behavior of underwater gas blowouts. The main objective is to investigate the unique features and quantitative measures in the gas jets that are classified in the sonic regime. The experimental conditions span the nominal Mach number from 0.8 to 3.34 and the Reynolds number of mass flow from 7.8×10^3 to 6.3×10^4.

We developed a series of image processing techniques to determine void fraction, jet trajectory, jet penetration length, jet expansion angle, water surface fountain profile, and bubble size distributions. Qualitative observation confirms the previous understanding of the behavior of underwater gas jets: strong pulsating releases with significant bubble breakup in the jet regime. Pinch-off events occur more often under low *Ma* than high *Ma* conditions and are usually located ~10× nozzle diameter within millisecond time scales.

The jet penetration length can be well described by a modified densimetric Froude number, which accounts for the real gas properties (velocity, pressure, density) at the release point. The measured gas trajectory can be estimated by the governing momentum equation, and the jet expansion angles are quite stable across all cases in our experiment.

Surface fountain profiles are found symmetric in shape on the gas release direction and can be described by Gaussian distribution. The data indicate they are a strong function of gas flow rate. The experimental data support a Froude number scaling, which can connect water surface observation to the dynamics of the release point.

The data show that bubble size distributions are quite similar, and the median bubble diameters are consistent across different cases ($d_{50} = 6.07 \sim 7.21$ mm). Our results extend the Weber number scaling by two orders of magnitude in predicting atomized bubble sizes in underwater gas blowout. The $-3/5$ scaling law is robust for estimating d_{50} in the sonic gas jet regime.

Data Availability Statement

All data are available from the corresponding author upon reasonable request.

Acknowledgments

The experiments and analyses are supported by the University of Missouri Research Council Grants and the National Science Foundation (Award No. 2049415). The corresponding author is also supported by the National Academy of Sciences Gulf Research Program's Early Career Research Fellowship.

Notation

The following symbols are used in this paper:

A = cross-sectional area of nozzle (L^2);
a = sound speed at gas phase (LT^{-1});
B = kinematic buoyancy flux (L^4T^{-3});
D = nozzle diameter (L);
Fr = densimetric Froude number $Fr=\sqrt{(\rho V_0^2)/((\rho-\rho_0)gD)}$;
Fr_m = modified densimetric Froude number $Fr_m=\sqrt{(\rho_g V_g^2+(P_g-P_0))/((\rho-\rho_g)gD)}$;
l_M = length scale of buoyant jets or plumes $l_M=Q^{3/4}/B^{1/2}$ (L);
l_p = measured jet penetration length (L);
M = kinematic momentum flux (L^4T^{-2});
M_g = gas momentum flux (MLT^2);
Ma = nominal Mach number $Ma=V_0/a$;
P_0 = hydrostatic pressure at the nozzle ($ML^{-1}T^{-2}$);
P_g = gas pressure at the nozzle ($ML^{-1}T^{-2}$);
Q = nominal flow rate at STP condition (L^3T^{-1});
Re_p = Reynolds number $Re_p=4w/\pi D\mu_g$;
V_0 = nominal velocity of gas (LT^{-1});
V_a = velocity scale as the velocity of receiving liquid $V_a=V_g\sqrt{\rho_g/\rho}$ (LT^{-1});
V_g = real gas velocity (LT^{-1});
We_p = modified Weber number $We_p=\rho_0 V_a^2 D/\sigma$;
w = mass flow rate (MT^{-1});
κ = specific heat ratio of gas;
μ_g = dynamic viscosity of gas ($ML^{-1}T^{-1}$);
ρ = density of water (ML^{-3});
ρ_0 = gas density under hydrostatic pressure at the nozzle (ML^{-3});
ρ_g = real gas density at the nozzle (ML^{-3});
σ = interfacial tension (MT^{-2}); and
χ = void fraction.

Supplemental Materials

Videos S1–S3 are available online in the ASCE Library (www.ascelibrary.org).

References

Asaeda, T., and J. Imberger. 1993. "Structure of bubble plumes in linearly stratified environments." *J. Fluid Mech.* 249 (4): 35–57. https://doi.org/10.1017/S0022112093001065.

Bandara, U. C., and P. D. Yapa. 2011. "Bubble sizes, breakup, and coalescence in deepwater gas/oil plumes." *J. Hydraul. Eng.* 137 (7): 729–738. https://doi.org/10.1061/(ASCE)HY.1943-7900.0000380.

Bombardelli, F., G. Buscaglia, C. Rehmann, L. Rincón, and M. García. 2007. "Modeling and scaling of aeration bubble plumes: A two-phase flow analysis." *J. Hydraul. Res.* 45 (5): 617–630. https://doi.org/10.1080/00221686.2007.9521798.

Carreau, J. L., F. Roger, L. Loukarfi, L. Gbahoue, and P. Hobbes. 1986. "Penetration of a horizontal gas jet submerged in a liquid." In *Proc., Intersociety Energy Conversion Engineering Conf.* Vienna, Austria: International Atomic Energy Agency.

Chanson, H. 2002. "Air-water flow measurements with intrusive, phase-detection probes: Can we improve their interpretation?" *J. Hydraul. Eng.* 128 (3): 252–255. https://doi.org/10.1061/(ASCE)0733-9429(2002)128:3(252).

Clift, R., J. Grace, and M. Weber. 1978. *Bubbles, drops, and particles*. London: Academic Press.

Cloete, S., J. E. Olsen, and P. Skjetne. 2009. "CFD modeling of plume and free surface behavior resulting from a sub-sea gas release." *Appl. Ocean Res.* 31 (3): 220–225. https://doi.org/10.1016/j.apor.2009.09.005.

Dissanayake, A., J. Gros, and S. Socolofsky. 2018. "Integral models for bubble, droplet, and multiphase plume dynamics in stratification and crossflow." *Environ. Fluid Mech.* 18 (Mar): 1167–1202. https://doi.org/10.1007/s10652-018-9591-y.

Dissanayake, A. L., J. A. DeGraff, P. D. Yapa, K. Nakata, Y. Ishihara, and I. Yabe. 2012. "Modeling the impact of co2 releases in Kagoshima bay, Japan." *J. Hydro-environ. Res.* 6 (3): 195–208. https://doi.org/10.1016/j.jher.2012.02.001.

Dissanayake, A. L., T. Nordam, and J. Gros. 2021a. "Simulations of subsea CO_2 leakage scenarios." In *Proc., Trondheim Conf. on CO_2 Capture, Transport and Storage*, 384–389. Trondheim, Norway: SINTEF Academic Press.

Dissanayake, A. L., M. Rezvani, S. A. Socolofsky, K. A. Bierlein, and J. C. Little. 2021b. "Bubble plume integral model for line-source diffusers in ambient stratification." *J. Hydraul. Eng.* 147 (5): 04021015. https://doi.org/10.1061/(ASCE)HY.1943-7900.0001885.

Ditmars, J. D., and K. Cederwall. 1974. "Analysis of air-bubble plumes." In *Proc., Coastal Engineering Conf.*, 2209–2226. Reston, VA: ASCE.

Fischer, H., E. List, R. Koh, J. Imberger, and N. Brooks. 1979. *Mixing in inland and coastal waters*. London: Academic Press.

Friedl, M., and T. Fannel. 2000. "Bubble plumes and their interaction with the water surface." *Appl. Ocean Res.* 22 (2): 119–128. https://doi.org/10.1016/S0141-1187(99)00022-X.

Grace, J. R., T. Wairegi, and J. Brophy. 1978. "Break-up of drops and bubbles in stagnant media." *Can. J. Chem. Eng.* 56 (1): 3–8. https://doi.org/10.1002/cjce.5450560101.

Gros, J., S. A. Socolofsky, A. L. Dissanayake, I. Jun, L. Zhao, M. C. Boufadel, C. M. Reddy, and J. S. Arey. 2017. "Petroleum dynamics in the sea and influence of subsea dispersant injection during deepwater horizon." *Proc. Natl. Acad. Sci. U.S.A.* 114 (38): 1006510070. https://doi.org/10.1073/pnas.1612518114.

Harby, K., S. Chiva, and J. Muñoz-Cobo. 2014. "An experimental investigation on the characteristics of submerged horizontal gas jets in liquid ambient." *Exp. Therm. Fluid Sci.* 53 (3): 26–39. https://doi.org/10.1016/j.expthermflusci.2013.10.009.

Hessenkemper, H., S. Starke, Y. Atassi, T. Ziegenhein, and D. Lucas. 2022. "Bubble identification from images with machine learning methods." *Int. J. Multiphase Flow* 155 (22): 104169. https://doi.org/10.1016/j.ijmultiphaseflow.2022.104169.

Hinze, J. O. 1955. "Fundamentals of the hydrodynamic mechanism of splitting in dispersion processes." *AIChE J.* 1 (3): 289–295. https://doi.org/10.1002/aic.690010303.

Hoefele, E., and J. Brimacombe. 1979. "Flow regimes in submerged gas injection." *Metall. Mater. Trans. B* 10 (Feb): 631–648. https://doi.org/10.1007/BF02662566.

Johansen, Ø. 2003. "Development and verification of deep-water blowout models." *Mar. Pollut. Bull.* 47 (9–12): 360–368. https://doi.org/10.1016/S0025-326X(03)00202-9.

Johansen, Ø., P. J. Brandvik, and U. Farooq. 2013. "Droplet breakup in subsea oil releases—Part 2: Predictions of droplet size distributions with and without injection of chemical dispersants." *Mar. Pollut. Bull.* 73 (1): 327–335. https://doi.org/10.1016/j.marpolbul.2013.04.012.

Johansen, Ø., H. Rye, A. G. Melbye, H. V. Jensen, B. Serigstad, and T. Knutsen. 2000. *Deep Spill JIP. Experimental Discharges of Gas and Oil at Helland Hansen—June 2000, Technical Report*. Trondheim, Norway: SINTEF Applied Chemistry.

Kim, Y., and H. Park. 2021. "Deep learning-based automated and universal bubble detection and mask extraction in complex two-phase flows." *Sci. Rep.* 11 (5): 8940. https://doi.org/10.1038/s41598-021-88334-0.

Lee, J. H., and V. Chu. 2003. *Turbulent jets and plumes: A Lagrangian approach*. Berlin: Springer.

Li, G., B. Wang, H. Wu, and S. F. DiMarco. 2020. "Impact of bubble size on the integral characteristics of bubble plumes in quiescent and unstratified water." *Int. J. Multiphase Flow* 125 (Apr): 103230. https://doi.org/10.1016/j.ijmultiphaseflow.2020.103230.

Li, X., G. Chen, and F. Khan. 2019. "Analysis of underwater gas release and dispersion behavior to assess subsea safety risk." *J. Hazard. Mater.* 367 (4): 676–685. https://doi.org/10.1016/j.jhazmat.2019.01.015.

Li, Z., M. Spaulding, D. French McCay, D. Crowley, and J. R. Payne. 2017. "Development of a unified oil droplet size distribution model with application to surface breaking waves and subsea blowout releases considering dispersant effects." *Mar. Pollut. Bull.* 114 (1): 247–257. https://doi.org/10.1016/j.marpolbul.2016.09.008.

Lim, H. J., K. A. Chang, C. B. Su, and C. Y. Chen. 2008. "Bubble velocity, diameter, and void fraction measurements in a multiphase flow using fiber optic reflectometer." *Rev. Sci. Instrum.* 79 (12): 125105. https://doi.org/10.1063/1.3053271.

Lima Neto, I. E., D. Z. Zhu, and N. Rajaratnam. 2008a. "Bubbly jets in stagnant water." *Int. J. Multiphase Flow* 34 (12): 1130–1141. https://doi.org/10.1016/j.ijmultiphaseflow.2008.06.005.

Lima Neto, I. E., D. Z. Zhu, and N. Rajaratnam. 2008b. "Effect of tank size and geometry on the flow induced by circular bubble plumes and water jets." *J. Hydraul. Eng.* 134 (6): 833–842. https://doi.org/10.1061/(ASCE)0733-9429(2008)134:6(833).

Martínez-Bazán, C., J. L. Montañés, and J. C. Lasheras. 1999. "On the breakup of an air bubble injected into a fully developed turbulent flow. part 1. breakup frequency." *J. Fluid Mech.* 401 (4): 157–182. https://doi.org/10.1017/S0022112099006680.

Masutani, S., and E. Adams. 2001. *Experimental study of multi-phase plumes with application to the deep ocean oil spills*. Washington, DC: Dept. of the Interior Minerals Management Service.

McNallan, M., and T. King. 1982. "Fluid dynamics of vertical submerged gas jets in liquid metal processing systems." *Metall. Mater. Trans. B* 13 (Jun): 165–173. https://doi.org/10.1007/BF02664573.

Milgram, J. H. 1983. "Mean flow in round bubble plumes." *J. Fluid Mech.* 133 (4): 345–376. https://doi.org/10.1017/S0022112083001950.

Milgram, J. H., and J. J. Burgess. 1984. "Measurements of the surface flow above round bubble plumes." *Appl. Ocean Res.* 6 (1): 40–44. https://doi.org/10.1016/0141-1187(84)90027-0.

Mori, K., Y. Ozawa, and M. Sano. 1982. "Characterization of gas jet behavior at a submerged orifice in liquid metal." *Trans. Iron Steel Inst. Japan* 22 (5): 377–384. https://doi.org/10.2355/isijinternational1966.22.377.

Nissanka, I. D., and P. D. Yapa. 2016. "Calculation of oil droplet size distribution in an underwater oil well blowout." *J. Hydraul. Res.* 54 (3): 307–320. https://doi.org/10.1080/00221686.2016.1144656.

Olsen, J. E., P. Skjetne, and S. T. Johansen. 2017. "Vles turbulence model for an Eulerian-Lagrangian modeling concept for bubble plumes." *Appl. Math. Modell.* 44 (1): 61–71. https://doi.org/10.1016/j.apm.2017.01.031.

Ozawa, Y., and K. Mori. 1983. "Characteristics of jetting observed in gas injection into liquid." *Trans. Iron Steel Inst. Japan* 23 (9): 764–768. https://doi.org/10.2355/isijinternational1966.23.764.

Premathilake, L. T., P. D. Yapa, I. D. Nissanka, and P. Kumarage. 2016. "Impact on water surface due to deepwater gas blowouts." *Mar. Pollut. Bull.* 112 (1): 365–374. https://doi.org/10.1016/j.marpolbul.2016.07.038.

Seol, D., T. Bhaumik, C. Bergmann, and S. Socolofsky. 2007. "Particle image velocimetry measurements of the mean flow characteristics in a bubble plume." *J. Eng. Mech.* 133 (4): 665–676. https://doi.org/10.1061/(ASCE)0733-9399(2007)133:6(665).

Simiano, M., R. Zboray, F. de Cachard, D. Lakehal, and G. Yadigaroglu. 2006. "Comprehensive experimental investigation of the hydrodynamics of large-scale, 3d, oscillating bubble plumes." *Int. J. Multiphase Flow* 32 (10–11): 1160–1181. https://doi.org/10.1016/j.ijmultiphaseflow.2006.05.014.

Socolofsky, S., T. Bhaumik, and D.-G. Seol. 2008. "Double-plume integral models for near-field mixing in multiphase plumes." *J. Hydraul. Eng.* 134 (8): 772–783. https://doi.org/10.1061/(ASCE)0733-9429(2008)134:6(772).

Themelis, N. J., P. Tarassoff, and J. Szekely. 1969. "Gas-liquid momentum transfer in a copper converter." *Trans. Met. Soc. AIME* 245 (14): 2425–2433.

Wang, B., C. Lai, and S. A. Socolofsky. 2019. "Mean velocity, spreading and entrainment characteristics of weak bubble plumes in unstratified and stationary water." *J. Fluid Mech.* 874 (5): 102–130. https://doi.org/10.1017/jfm.2019.461.

Wang, B., and S. A. Socolofsky. 2015a. "A deep-sea, high-speed, stereoscopic imaging system for in situ measurement of natural seep bubble and droplet characteristics." *Deep Sea Res. Part I* 104 (5): 134–148. https://doi.org/10.1016/j.dsr.2015.08.001.

Wang, B., and S. A. Socolofsky. 2015b. "On the bubble rise velocity of a continually released bubble chain in still water and with crossflow." *Phys. Fluids* 27: 103301. https://doi.org/10.1063/1.4932176.

Wang, B., S. A. Socolofsky, J. A. Breier, and J. S. Seewald. 2016. "Observation of bubbles in natural seep flares at MC 118 and GC 600 using in situ quantitative imaging." *J. Geophys. Res. Ocean* 121 (3): 2203–2230. https://doi.org/10.1002/2015JC011452.

Wang, B., S. A. Socolofsky, C. C. Lai, E. E. Adams, and M. C. Boufadel. 2018. "Behavior and dynamics of bubble breakup in gas pipeline leaks and accidental subsea oil well blowouts." *Mar. Pollut. Bull.* 131 (4): 72–86. https://doi.org/10.1016/j.marpolbul.2018.03.053.

Weiland, C., and P. P. Vlachos. 2013. "Round gas jets submerged in water." *Int. J. Multiphase Flow* 48 (Jan): 46–57. https://doi.org/10.1016/j.ijmultiphaseflow.2012.08.002.

Wu, H., B. Wang, S. F. DiMarco, and L. Tan. 2021. "Impact of bubble size on turbulent statistics in bubble plumes in unstratified quiescent water." *Int. J. Multiphase Flow* 141 (Aug): 103692. https://doi.org/10.1016/j.ijmultiphaseflow.2021.103692.

Wuest, A., N. H. Brooks, and D. M. Imboden. 1992. "Bubble plume modeling for lake restoration." *Water Resour. Res.* 28 (12): 3235–3250.

Yapa, P. D., L. K. Dasanayaka, U. C. Bandara, and K. Nakata. 2010. "A model to simulate the transport and fate of gas and hydrates released in deepwater." *J. Hydraul. Res.* 48 (5): 559–572. https://doi.org/10.1080/00221686.2010.507010.

Yapa, P. D., and L. Zheng. 1997. "Simulation of oil spills from underwater accidents. 1. Model development." *J. Hydraul. Res.* 35 (5): 673–688. https://doi.org/10.1080/00221689709498401.

Zhao, L., M. C. Boufadel, E. Adams, S. A. Socolofsky, T. King, K. Lee, and T. Nedwed. 2015. "Simulation of scenarios of oil droplet formation from the deepwater horizon blowout." *Mar. Pollut. Bull.* 101 (1): 304–319. https://doi.org/10.1016/j.marpolbul.2015.10.068.

Zhao, L., M. C. Boufadel, K. Lee, T. King, N. Loney, and X. Geng. 2016. "Evolution of bubble size distribution from gas blowout in shallow water." *J. Geophys. Res. Oceans* 121 (3): 1573–1599. https://doi.org/10.1002/2015JC011403.

Zhao, Y., and G. Irons. 1990. "The breakup of bubbles into jets during submerged gas injection." *Metall. Mater. Trans. B* 21 (Feb): 997–1003. https://doi.org/10.1007/BF02670270.

Zheng, L., P. D. Yapa, and F. Chen. 2003. "A model for simulating deepwater oil and gas blowouts—Part I: Theory and model formulation." *J. Hydraul. Res.* 41 (4): 339–351. https://doi.org/10.1080/00221680309499980.